CHEMISTRY
A EUROPEAN JOURNAL

DOI: 10.1002/chem.201000562

Highly Ordered Mesoporous Cobalt Oxide Nanostructures: Synthesis, Characterisation, Magnetic Properties, and Applications for Electrochemical Energy Devices

Guoxiu Wang,*[a] Hao Liu,[b] Josip Horvat,[b] Bei Wang,[a] Shizhang Qiao,[c] Jinsoo Park,[d] and Hyojun Ahn[d]

Abstract: Highly ordered mesoporous Co_3O_4 nanostructures were prepared using KIT-6 and SBA-15 silica as hard templates. The structures were confirmed by small angle X-ray diffraction, high resolution transmission electron microscopy, and N_2 adsorption–desorption isotherm analysis. Both KIT-6 cubic and SBA-15 hexagonal mesoporous Co_3O_4 samples exhibited a low Néel temperature and bulk antiferromagnetic coupling due to geometric confinement of antiferromagnetic order within the nanoparticles. Mesoporous Co_3O_4 electrode materials have demonstrated the high lithium storage capacity of more than $1200\,mAh\,g^{-1}$ with an excellent cycle life. They also exhibited a high specific capacitance of $370\,F\,g^{-1}$ as electrodes in supercapacitors.

Keywords: cobalt · fuel cells · lithium ion battery · magnetic properties · mesoporous materials · supercapacitor

Introduction

Mesoporous structures have been extensively investigated due to their widespread applications such as support for catalysts, gas sensors, electrode materials for batteries, supercapacitors, and fuel cells, sorbants for separation, and media for gas storage and drug delivery.[1–6] Owing to their high specific surface area, large pore volume, periodically distributed pores, and peculiar surface properties, ordered mesoporous functional materials have demonstrated many unique chemical and physical properties. In general, mesoporous structures can be synthesized by either the soft template or hard template methods through a process called nanocasting. In a nanocasting process, the voids of templates are filled with the material to be cast. After the removal of the template, a replica of the mesoporous structure can be obtained, which is the negative replica in the case of one time casting.[7] Soft templates usually yield mesoporous structures with low order and low crystallinity.[8,9] The hard template method has many advantages over the soft template method such as controllability, pore regularity, and crystallinity, that is, it can produce highly ordered mesoporous materials with crystalline walls.[10–12] Many types of mesoporous metal oxides have been developed using mesoporous silica templates, such as MCM-41, SBA-15, and KIT-16 in the past decade.[13–17] However, the successful synthesis of mesoporous metal oxide materials still largely depends on the control and manipulation of the preparation conditions.

Lithium ion batteries and supercapacitors are important electrochemical energy storage and conversion devices. Currently, lithium ion batteries are the dominant power sources for portable electronic devices.[18–20] The combination of lithium ion batteries and supercapacitors represents an advanced power supply for hybrid and plug-in hybrid electric

[a] Prof. Dr. G. Wang, B. Wang
Department of Chemistry and Forensic Science
University of Technology Sydney
Sydney, NSW 2007 (Australia)
Fax: (+61) 295141460
E-mail: Guoxiu.Wang@uts.edu.au

[b] H. Liu, Prof. J. Horvat
School of Mechanical, Materials and
Mechatronic Engineering and Institute for Superconducting
and Electronic Materials, University of Wollongong
Wollongong, NSW 2522 (Australia)

[c] Prof. Dr. S. Qiao
ARC Centre of Excellence for Functional Nanomaterials, Australian
Institute for Bioengineering and Nanotechnology, The University of
Queensland, QLD 4072 (Australia)

[d] J. Park, Prof. Dr. H. Ahn
School of Materials Science and Engineering
Gyeongsang National University, 900 Gazwa-dong, Jinju
Gyeongnam 660-701 (Korea)

Supporting information for this article is available on the WWW under http://dx.doi.org/10.1002/chem.201000562.

vehicles, and an advanced energy storage sources in solar and wind electricity generation systems. These power applications urgently require us to develop new electrode materials with high capacity (in particular, high rate capacity) and high energy density. Mesoporous structures (with pore sizes in the range of 2–5 nm) provide a unique 3D framework architecture as electrode materials for lithium ion batteries and supercapacitors.[21–24] Transition-metal oxides have exhibited high capacity for reversible lithium storage based on the so called "conversion" reaction, which was first reported by Poizot et al.[25] Among them, cobalt oxide has demonstrated the best electrochemical performance in terms of specific capacity and cyclability.[26] On the other hands, nanosize Co_3O_4 has also exhibited high capacitance as electrode in supercapacitors.[27]

Herein, we report the facile synthesis of two types of highly ordered mesoporous Co_3O_4 materials with cubic *Ia3d* structure prepared from KIT-6 silica templates and hexagonal *P6mm* structure prepared from SBA-15 silica templates, respectively. These two types of mesoporous cobalt oxides showed ferromagnetic ordering even at room temperature and excellent electrochemical performance as electrode materials in lithium ion batteries and supercapacitors.

Results and Discussion

Structure and morphology characterisation: Figure 1a) and b) presents the small angle X-ray diffraction (SAXRD) patterns of cubic mesoporous Co_3O_4 (replicas of KIT-6) and hexagonal mesoporous Co_3O_4 (replicas of SBA-15), respectively. In Figure 1a), the SAXRD peak at 0.94° corresponds to the (211) diffraction of the cubic *Ia3d* mesoporous structure, while the SAXRD peaks in Figure 1b) can be assigned to (100), (110) and (200) diffraction lines of the hexagonal mesoporous structure (*P6mm*). SAXRD diffraction peaks of the patterns should be attributed to long range regularity, namely the highly ordered mesoporous structures of the two types of cobalt oxides.[28] The wide-angle XRD patterns are shown as insets in Figure 1a) and b), respectively. All diffraction lines can be readily indexed to the face-centered cubic phase (*Fd3m*, JCPDS card No. 76-1802), indicating that Co_3O_4 has been crystallized within the mesopores both in KIT-6 and in SBA-15 templates. This has been further confirmed by the high-resolution transmission electron microscope (HRTEM) analysis.

Two types of mesoporous Co_3O_4 were analyzed by transmission electron microscope (TEM) and high resolution TEM (HRTEM) analysis, which confirmed the highly ordered mesoporous structure and high crystallization degree. Figure 2a)–d) shows TEM and HRTEM images of KIT-6 mesoporous Co_3O_4. Figure 2a) is a low magnification TEM image, from which the sizes of individual mesoporous particles can be determined to be around 100 nm. Selected area electron diffraction (SAED) was performed on the mesoporous particle marked with a circle and is shown as the inset in Figure 2a). It exhibits a single-crystal-like diffraction pattern, implying that the walls in the mesoporous structure are highly crystalline with a near single-crystal arrangement of atoms within the walls over the entire mesoporous particle.[29] Figure 2b) shows a magnified TEM view of the mesoporous structure recorded along the [111] direction, from which highly ordered and regular mesopores are clearly visible. Figure 2c) and d) further presents HRTEM and lattice-resolved HRTEM images of KIT-6 mesoporous Co_3O_4, in which two *d* spacings of the (111) and (220) crystal planes of Co_3O_4 are indexed, explicitly illustrating the highly crystalline nature of the walls of mesoporous Co_3O_4. SBA-15 mesoporous Co_3O_4 exhibits nanowire structures (as shown in Figure 3a–d), which are derived from the parallel cylindrical pores in the SBA-15 template. Figure 3a) illustrates a general TEM view of mesoporous Co_3O_4 nanowires. We notice that individual nanowires are organized into parallel bundles with sizes in the range of a few hundred nanometers. The SAED pattern of a nanowire bundle marked with a circle in Figure 3a) is shown in Figure 3b). The ring diffraction pattern indicates the polycrystalline nature of the mesoporous nanowires, which can be fully indexed to cubic *Fd3m* Co_3O_4 phase. Figure 3c) exhibits a magnified view of a mesoporous Co_3O_4 bundle, and its corresponding fast Fourier transform (FFT) pattern is shown as the inset in Figure 3c). The FFT is

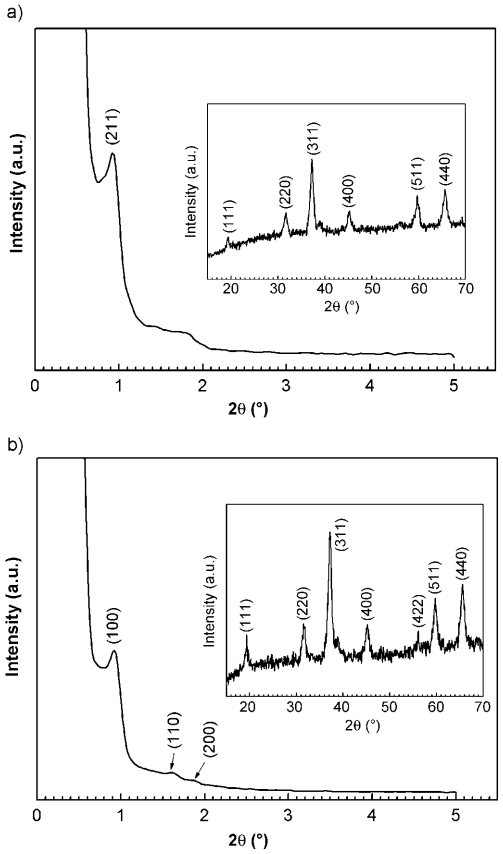

Figure 1. Small angle X-ray diffraction (SAXRD) patterns of a) cubic mesoporous Co_3O_4 (replicas of KIT-6) and b) hexagonal mesoporous Co_3O_4 nanowires (replicas of SBA-15). The insets are the corresponding wide angle X-ray diffraction patterns.

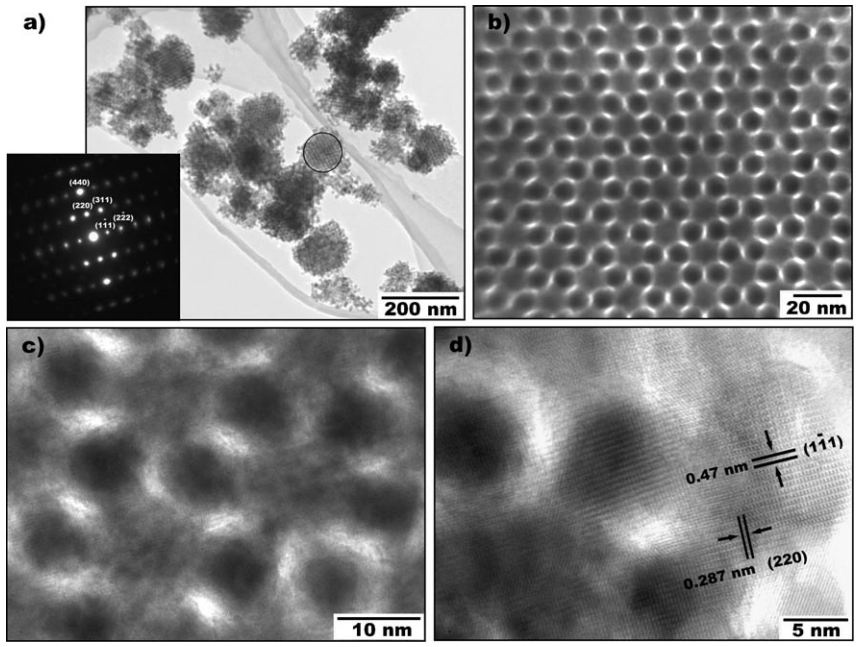

Figure 2. a) Low magnification TEM image of KIT-6 mesoporous Co_3O_4, in which the inset is the corresponding SAED pattern. b) High magnification TEM image of KIT-6 mesoporous Co_3O_4, showing highly ordered mesopores. c) and d) HRTEM images show the lattices of the crystalline walls of KIT-6 mesoporous Co_3O_4.

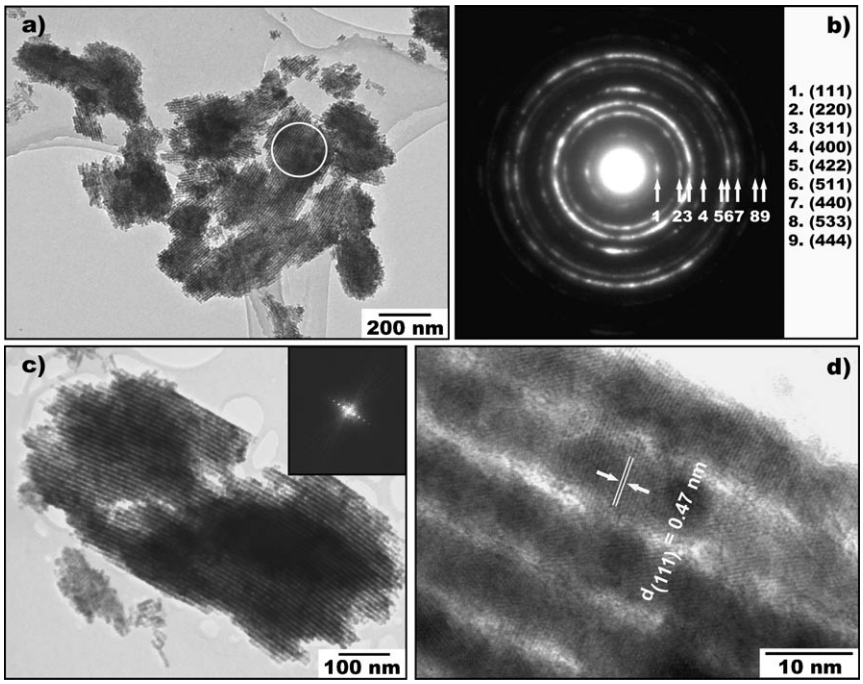

Figure 3. a) A general TEM image of SBA-15 mesoporous Co_3O_4 nanowires. b) A SAED pattern of a nanowire bundle, showing the polystalline nature of the nanowires. c) A high magnification TEM image of a mesoporous Co_3O_4 nanowire bundles. The inset is the corresponding FFT pattern. d) A HRTEM image of the mesoporous Co_3O_4 nanowire structure.

simply an inverse form of the entire nanowire bundle, in which the spots reflect the highly ordered arrangement of parallel nanowires. Figure 3d) shows a HRTEM image of the mesoporous Co_3O_4 nanowire structure. Nanoparticles with a size of about 5–6 nm are regularly aggregated to form individual nanowires. The (111) lattice planes with a d spacing of 0.47 nm are clearly distinguishable in Figure 3d). Mesopores exist between the individual nanowires.

The pore sizes, their distribution and the Brunauer–Emmett–Teller (BET) surface areas of the two types of mesoporous Co_3O_4 were examined via nitrogen adsorption-desorption measurements. Figure 4 shows the typical type IV isotherms with type H1 hysteresis loops defined by IUPAC,[30] which are characteristic of mesostructures with cylindrical or *Ia3d* channels. The pore size distribution curves are presented as the insets in Figure 4a) and b). The average pore sizes for cubic Co_3O_4 and hexagonal mesoporous Co_3O_4 are 3.32 and 4.16 nm, respectively. The BET surface areas are 126.2 $m^2 g^{-1}$ for cubic mesoporous Co_3O_4 and 110.4 $m^2 g^{-1}$ for hexagonal mesoporous Co_3O_4, which were deduced from the nitrogen adsorption–desorption measurements. Therefore, SAXRD, TEM, HRTEM, and IV isotherm measurements have unambiguously confirmed the highly ordered nature of the mesoporous Co_3O_4 structures synthesized by the hard template method.

Zero-field cooled (ZFC) and field cooled (FC) measurement of the magnetic moments of the two types of mesoporous Co_3O_4 samples are shown in Figure 5 (solid line for KIT-6 cubic sample and dashed line for SBA-15 nanowire sample). The main feature of these measurements is a cusp at the characteristic Néel temperature, T_N, corresponding to the onset of antiferromagnetic ordering below this temperature.[31] Above the Néel temperature T_N, the ZFC and FC measurements for each of the samples overlap, whereas, they do not overlap below T_N. Both samples show the signature of paramag-

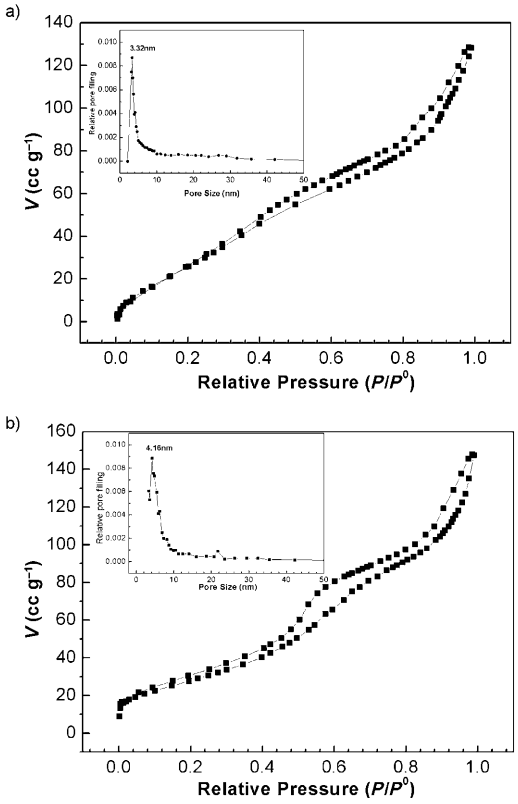

Figure 4. N_2 sorption isotherms of mesoporous Co_3O_4 a) KIT-6 type, b) SBA-15 type. The insets are pore size distribution curves.

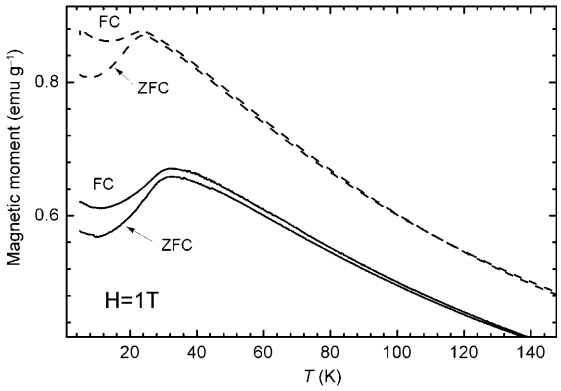

Figure 5. Temperature dependence of ZFC and FC magnetic moment for KIT-6 mesoporous Co_3O_4 (——: T_N = 32.2 K) and SBA-15 mesoporous Co_3O_4 (-----: T_N = 23.7 K) nanowire samples.

netic phase above T_N, even though the measurements cannot be fitted to the Curie–Weiss law over the whole temperature range above T_N. The fit is acceptable only above ~150 K. The observed cusp does not correspond to freezing of superparmagnetic particles or spin freezing.[32] Our mesoporous samples were too large to exhibit superparamagnetism, as was observed for Co_3O_4 nanoparticles 3 nm in diameter.[33] If either of these two effects were occurring in our samples above 20 K, the cusp would be observed only in the ZFC measurements. FC measurements would give a constant magnetic moment below the freezing temperatures as the spins aligned by the magnetic field were frozen in.

The values of T_N for the mesoporous KIT-6 cubic sample and the SBA-15 nanowire sample were 32.3 and 23.7 K, respectively. Macroscopic Co_3O_4 crystals give T_N of 40 K.[31,34] However, geometric confinement of magnetic ordering in nanoparticles results in lowering of T_N, which can be described by:[35]

$$\Delta T_N = T_{N0}\left(\frac{\xi_0}{d}\right)\lambda \quad (1)$$

where ΔT_N, T_{N0}, ξ_0, λ and d are $T_{N0}-T_N$, Néel temperature for infinite crystal, correlation length of the magnetic ordering, shift exponent and diameter of the nanoparticle, respectively. The values of $\lambda=1.1$ and $\xi_0=2.8$ nm were reported for Co_3O_4 nanoparticles.[36] Equation (1) gives the value of d for mesoporous KIT-6 and SBA-15 nanowire samples as 12.5 and 6.3 nm, respectively. This is in good agreement with the size of individual crystallites observed by TEM. A decrease in the magnetic moment with temperature below 10 K can also be observed in Figure 5. This is probably due to spin freezing at these low temperatures, as reported by Takada et al.[33]

Another interesting feature of ZFC and FC measurements is that the magnetic moment per unit mass of the Co_3O_4 sample with hexagonal mesostructure is 1.2 times higher than that of the Co_3O_4 sample with *Ia3d* mesostructure in the region of $T>50$ K. This is probably associated with the unpaired spins at the surface of the nanoparticles. Because these spins do not experience antiferromagnetic coupling to the outside of the nanoparticles, they are easier to align with magnetic field above T_N against thermal excitations than the bulk spins. Even though thermal excitations overcome the antiferromagnetic coupling above T_N, the antiferromagnetic interaction still exists between the spins. Because of the different size of the nanocrystals in the two samples, where the KIT-6 mesoporous Co_3O_4 sample has a single crystal-like structure with mesopores inside and a size ranging up to more than 100 nm, which is much larger than that of the individual nanocrystals in the SBA-15 Co_3O_4 nanowire sample, the SBA-15 Co_3O_4 nanowire sample is expected to have more surface spins per unit weight, which are easy to align with an external field, resulting in the observed larger magnetic moment in Figure 5.

Magnetic hysteresis loops measured between 5 and 300 K reveal a linear dependence of magnetic moment on the field (Figure 6). The magnetic moment per unit mass of the SBA-15 Co_3O_4 nanowires is again 1.2 times higher than that for the KIT-6 mesoporous Co_3O_4 sample. This is in agreement with the ZFC and FC measurements at constant field. Only a slight deviation from linearity of the hysteresis loops is observed around $H=0$, where hysteresis loops are visible after zooming-in at all temperatures. This is more obvious at low temperatures. Magnetic hysteresis loops of the KIT-6 mesoporous Co_3O_4 sample in full range of the fields are shown in Figure S1 in the Supporting Information.

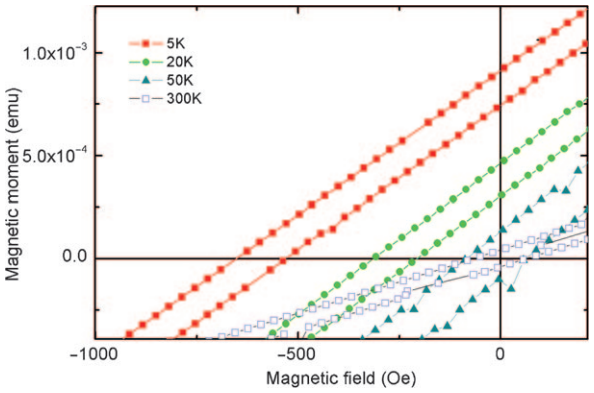

Figure 6. Magnetic hysteresis loops measured between 5 and 300 K. For each pair, the upper-left line is the KIT-6 mesoporous Co_3O_4 sample and the down-right line is the SBA-15 mesoporous nanowire Co_3O_4 sample.

The hysteresis loops of the SBA-15 nanowire sample showed the same trend. All of the hysteresis loops have a non-zero coercive field H_c (Figure 7), indicating a ferromagnetic ordering of the unpaired surface spins. This is in addition to the antiferromagnetic ordering of bulk spins. The SBA-15 Co_3O_4 nanowire sample has a larger coercive field than the KIT-6 mesoporous Co_3O_4 samples. This is to be expected because the smaller crystallites in the nanowires have more defects that impede changes in magnetization arising from the external field and therefore give a larger H_c. Both samples show a decrease in H_c with cooling at and below T_N. This is associated with the exchange interaction between the ferromagnetic surface spins and the bulk antiferromagnetic spins.[37] Further increase of H_c with cooling below 10 K is due to spin-freezing mechanisms.

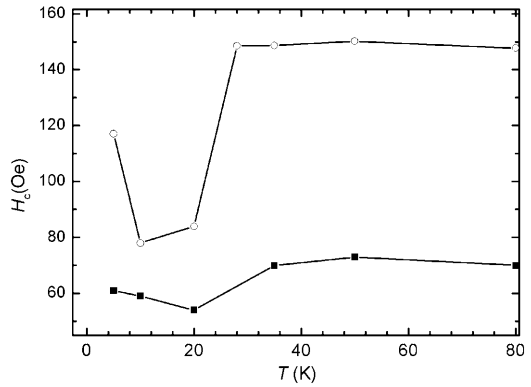

Figure 7. Temperature dependence of the coercive field for the two types of mesoporous Co_3O_4 samples (KIT-6: ■, SBA-15: ○).

A clear evidence for the exchange bias of ferromagnetically coupled surface spins is provided by the shift of the hysteresis loops to negative field.[36] The center of the hysteresis loop is shifted by field H_s, as shown in Figure 8. The shift vanishes above T_N for both samples, clearly showing the decisive role of antiferromagnetic bulk spins in the shift of hysteresis loops.

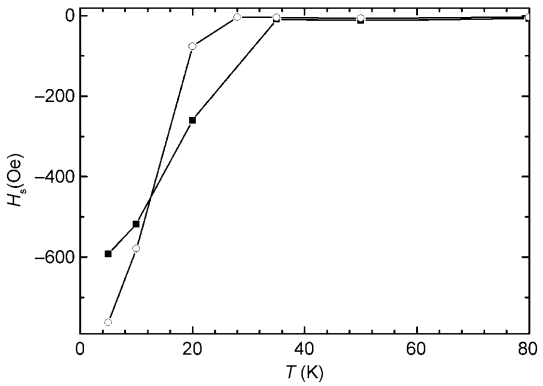

Figure 8. Temperature dependence of the field of the centre of magnetic hysteresis loops, showing the shift of the hysteresis loop along the field-axis, which occurs because of the exchange bias of ferromagnetically ordered surface spins through their coupling to the antiferromagnetically ordered bulk spins (KIT-6: ■, SBA-15: ○).

The electrochemical performance of the two types of as-prepared Co_3O_4 mesoporous samples in lithium ion cells were evaluated by cyclic voltammetry (CV) and galvanostatic charge/discharge tests. The CV curves of the mesoporous KIT-6 Co_3O_4 electrode are shown in Figure 9a). In the first scanning cycle, there is a reduction peak at 0.8 V, which is associated with the formation of a solid electrolyte interphase (SEI) layer on the surface of the electrode, but disappears from the second cycle. Two stable reduction peaks appear during cathodic polarization, which is related to multistep reduction of Co_3O_4 to CoO and metallic Co. An anodic peak at 2.2 V corresponds to the oxidation of the reduced Co to Co^{n+}. Figure 9b) shows the discharge and charge curves of mesoporous KIT-6 Co_3O_4 electrode at a current rate of 50 $mA g^{-1}$. In the first cycle, the electrode delivered a lithium storage capacity of 1760 $mA h g^{-1}$, which is similar to what has been previously reported for porous Co_3O_4 nanotubes and nanoneedles.[38–40] From the second cycle, the mesoporous Co_3O_4 electrode maintained a high reversible capacity above 1200 $mAh g^{-1}$ with high coulombic efficiency. Mesoporous Co_3O_4 electrode exhibited a capacity higher than the theoretical capacity of Co_3O_4 (890 $mAh g^{-1}$). This could be attributed to high surface area and interconnected porous structures, which provide extra active sites for Li^+ storage.[41]

We also performed charge/discharge cycling test at different current rates; the results are shown in Figure 10. The KIT-6 mesoporous Co_3O_4 electrodes demonstrated superior electrochemical performance. Even at high current density of 300 $mA g^{-1}$, the mesoporous electrode exhibited almost the same specific capacity as at low current density. Recently, mesoporous Co_3O_4 nanobelts was reported to deliver 1400 $mAh g^{-1}$ capacity at a low current rate of 40 $mAh g^{-1}$.[41] However, long-term cyclability and high-current performance are not clear. The extraordinary performance of our mesoporous Co_3O_4 material should be attributed to the highly ordered mesoporous structure, in which the electrolyte can easily diffuse into the mesopores. On the

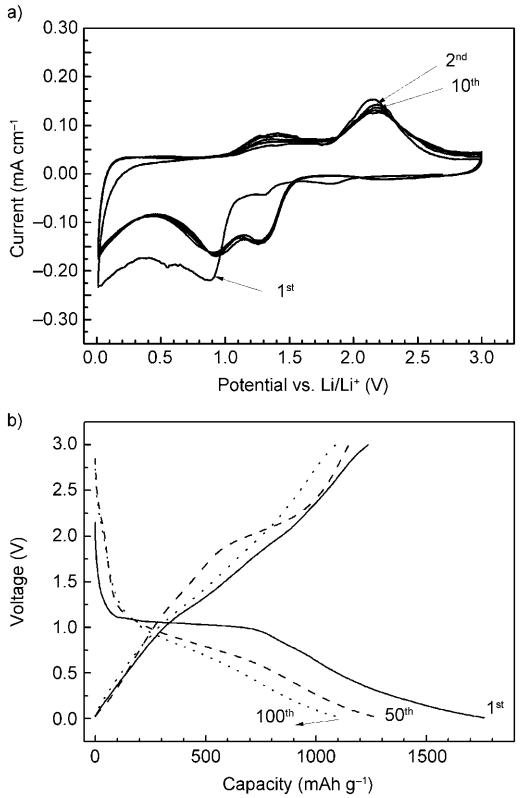

Figure 9. a) Cyclic voltammograms of the KIT-6 mesoporous Co_3O_4 electrode. b) Discharge and charge profiles of the KIT-6 mesoporous Co_3O_4 electrode in lithium-ion cells.

other hand, the thin walls in the mesoporous structure (a few nm) provide a short path for lithium ion diffusion and migration, therefore inducing excellent electrochemical performance. The performances of the SBA-15 mesoporous Co_3O_4 nanowire electrodes were also systematically investigated and the corresponding results are shown in Figures S2 and S3. They exhibited similar electrochemical behavior to that of the KIT-6 mesoporous Co_3O_4 electrodes.

Since mesoporous Co_3O_4 materials have large specific surface area, they are ideal electrode materials for supercapacitors. The capacitances of the two types of mesoporous Co_3O_4 electrodes were evaluated by cyclic voltammetry measurements. Figure 11a) and b) show the CV curves obtained at different scanning rates for the KIT-6 mesoporous Co_3O_4 electrode and the SBA-15 mesoporous Co_3O_4 nanowire electrode, respectively. All CV curves exhibited a broad oxidation peak and a sharp reduction peak rather than the ideally rectangular shape. This characteristic indicates that the supercapacitance was not double layer capacitance, but originated from faradaic pseudocapacitance. The maximum specific capacitances were deduced from the CV curves to be 282 and 370 $F g^{-1}$ for the KIT-6 mesoporous Co_3O_4 and the SBA-15 mesoporous Co_3O_4 nanowires, respectively. Therefore, the SBA-15 mesoporous Co_3O_4 nanowires exhibited much higher capacitance than for previously reported nanoporous Co_3O_4 nanorods.[27]

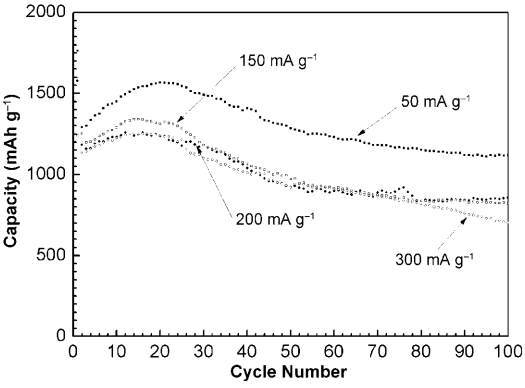

Figure 10. Reversible lithium storage capacity vs cycle number for the KIT-6 mesoporous Co_3O_4 electrode at different current rates.

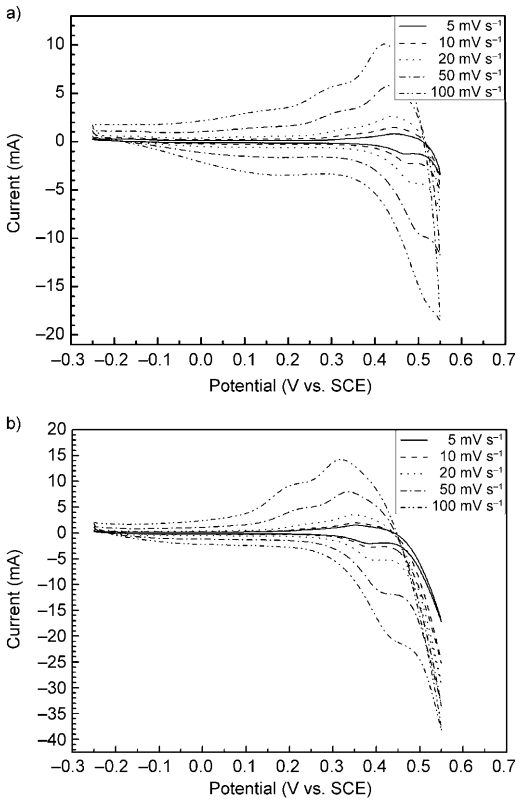

Figure 11. Cyclic voltammetry of mesoporous Co_3O_4 as electrodes in supercapacitors at different scanning rates: a) the KIT-6 mesoporous Co_3O_4 sample and b) the SBA-15 mesoporous Co_3O_4 nanowire sample.

Conclusion

In conclusion, we have synthesized two types of mesoporous Co_3O_4, one with a KIT-6 cubic structure and the other with an SBA-15 hexagonal structure. Small angle X-ray diffraction, TEM, HRTEM, and IV N_2 sorption analysis revealed the highly ordered mesoporous structures of the as-prepared products. Both the KIT-6 mesoporous and the SBA-15

Co_3O_4 nanowire samples exhibit bulk antiferromagnetic coupling below $T_N = 32.3$ and 23.7 K, respectively. Lowering of T_N from its value of 40 K was observed due to geometric confinement of antiferromagnetic order within nanoparticles. The unpaired surface spins contribute to a second type of magnetic ordering. These spins couple ferromagnetically, giving a small magnetic hysteresis loop. The ferromagnetically ordered surface spins are also coupled to the antiferromagnetically ordered bulk spins, resulting in exchange bias and shift of the ferromagnetic hysteresis loop. When used as anodes for lithium storage in lithium ion cells, mesoporous Co_3O_4 electrodes demonstrated excellent electrochemical performance. Mesoporous Co_3O_4 electrodes also exhibited a high supercapacitance of 370 $F g^{-1}$ as electrode materials in supercapacitors.

Experimental Section

Synthesis of mesoporous Co_3O_4: The KIT-6 and SBA-15 SiO_2 templates were synthesized according to previous reports.[16,17] The mesoporous Co_3O_4 replicas from the 3D cubic KIT-6 and the 2D hexagonal SBA-15 were obtained by a hard template method.[10] Typically, 3–6 mmol $Co(NO_3)_2{\cdot}6H_2O$ was dissolved in ethanol (15–30 mL) to form a transparent solution. Then, dry SBA-15 or KIT-6 (0.45 g) was added to the solution. After stirring for 12 h, the solvent was removed by evaporation at room temperature. The dry powder was ground and sintered at 400 °C for 2 h to decompose the nitrate. The impregnation step was repeated one more time to obtain cobalt precursor/SiO_2 composites. After the final calcination at 600 °C for 6 h, the silica templates were removed by stirring twice with 2 M hot sodium hydroxide solution and then the final mesoporous Co_3O_4 was obtained after washing by de-ionized water and drying at 50 °C.

Materials characterization: SAXRD patterns were collected on a Bruker D8 Advanced X-ray diffractometer using $Cu_{K\alpha}$ radiation. N_2 adsorption–desorption isotherms were obtained using a Quadrasorb SI analyzer at 77 K. Brunauer–Emmett–Teller (BET) surface area was calculated using experimental points at a relative pressure of $P/P_0 = 0.05$–0.25. The pore size distribution was calculated by the Barret–Joyner–Halenda (BJH) method. The porous structure and crystal structures of mesoporous Co_3O_4 samples were characterized by TEM and HRTEM analysis (JEOL 2011 TEM facility). Measurements of magnetic moment were performed at different fields and temperatures, using a Vibrating Sample Magnetometer of a Quantum Design Physical Property Measurement System. The frequency and amplitude of the sample vibration were 40 Hz and 2 mm, respectively. Measurements of the temperature dependence of the magnetic moment in the ZFC regime were performed by first cooling the sample down to 5 K in Earth's field. A persistent field of 1 T was applied at 5 K, and the magnetic moment was measured in this field upon warming to 300 K. In the FC regime, samples were measured in 1 T field upon cooling from 300 to 5 K. The sweep rate of the temperature was kept at 1 K per minute. Magnetic hysteresis loops were measured at selected temperatures with a constant sweep rate of the field of 50 Oe s^{-1}.

Electrochemical testing: Mesoporous Co_3O_4 powders were mixed with a binder, poly(vinylidene fluoride) (PVdF), and carbon black at weight ratios of 60:10:30 in *N*-methyl-2-pyrrolidone (NMP) solvent to form a slurry. Then, the resultant slurry was uniformly pasted on Cu foil substrates with a blade. These prepared electrode sheets were dried at 100 °C in a vacuum oven for 12 h and pressed under a pressure of approximately 200 $kg cm^{-2}$. CR2032-type coin cells were assembled in a glove box for electrochemical characterization. The electrolyte was 1 M $LiPF_6$ in a 1:1 mixture of ethylene carbonate and dimethyl carbonate. Li metal foil was used as the counter and reference electrode. The cells were galvanostatically charged and discharged at different current densities within the range of 0.01 to 3.0 V. Cyclic voltammetry (CV) curves were measured at 0.1 mV s^{-1}within the range of 0.01–3.0 V using an electrochemistry workstation (CHI660C). For supercapacitance measurements, a beaker-type three-electrode cell was fabricated utilizing mesoporous Co_3O_4 as the electrode material. The electrochemical properties were evaluated in 2 M KOH electrolyte at room temperature by the cyclic voltammetry (CV) method on an electrochemical workstation (CHI 660C). Platinum foil and a saturated calomel reference electrode (SCE) were used as the counter electrode and the reference electrode, respectively. CV measurements were conducted over the voltage range from −0.25 to 0.55 V at various scan rates (5, 10, 20, 50, and 100 mV s^{-1}).

Acknowledgements

This work was financially supported by the Australian Research Council (ARC) through the ARC Discovery project (DP0772999) and the National Research Foundation of Korea through the WCU (World Class University) Program (R32-2008-000-20093-0).

[1] A. Firouzi, D. J. Schaefer, S. H. Tolbert, G. D. Stucky, B. F. Chemelka, *J. Am. Chem. Soc.* **1997**, *119*, 9466.
[2] P. D. Yang, T. Deng, D. Y. Zhao, P. Y. Feng, D. Pine, B. F. Chemelka, G. M. Whitesides, G. D. Stucky, *Science* **1998**, *282*, 2244.
[3] C. D. Liang, Z. J. Li, S. Dai, *Angew. Chem.* **2008**, *120*, 3754; *Angew. Chem. Int. Ed.* **2008**, *47*, 3696.
[4] S. M. Zhu, H. S. Zhou, T. Miyoshi, M. Hibino, I. Honma, M. Ichihara, *Adv. Mater.* **2004**, *16*, 2012.
[5] Y. L. Zhang, S. W. Zha, M. L. Liu, *Adv. Mater.* **2005**, *17*, 487.
[6] L. Zhang, S. H. Qiao, Y. G. Jin, Z. G. Chen, H. C. Gu, G. Q. Lu, *Adv. Mater.* **2008**, *20*, 805.
[7] Y. Q. Wang, C. M. Yang, W. Schmidt, B. Spliethoff, E. Bill, F. Schüth, *Adv. Mater.* **2005**, *17*, 53.
[8] D. Y. Zhao, Q. S. Huo, J. L. Feng, B. F. Chemlka, G. D. Stucky, *J. Am. Chem. Soc.* **1998**, *120*, 6024.
[9] G. J. D. Soler-Illia, C. Sanchez, B. Lebeau, J. Patarin, *Chem. Rev.* **2002**, *102*, 4093.
[10] B. Z. Tian, X. Y. Liu, H. F. Yang, S. H. Xie, C. Z. Yu, B. Tu, D. Y. Zhao, *Adv. Mater.* **2003**, *15*, 1370.
[11] F. Jiao, A. Harrison, J. C. Jumas, A. V. Chadwick, W. Kockelman, P. G. Bruce, *J. Am. Chem. Soc.* **2006**, *128*, 5468.
[12] X. Y. Lai, X. T. Li, W. C. Geng, J. C. Tu, J. X. Li, S. L. Qiu, *Angew. Chem.* **2007**, *119*, 752; *Angew. Chem. Int. Ed.* **2007**, *46*, 738.
[13] M. Imperor-Clerc, D. Bazin, M. D. Appay, P. Beaunier, A. Davidson, *Chem. Mater.* **2004**, *16*, 1813.
[14] C. Dickinson, W. Zhou, R. P. Hodgkins, Y. Shi, D. Zhao, H. He, *Chem. Mater.* **2006**, *18*, 3088.
[15] R. Ryoo, S. H. Joo, S. Jun, *J. Phys. Chem. B* **1999**, *103*, 7743.
[16] C. Z. Yu, J. Fan, B. Z. Tian, D. Y. Zhao, G. D. Stucky, *Adv. Mater.* **2003**, *15*, 1742.
[17] F. Kleitz, S. H. Choi, R. Ryoo, *Chem. Commun.* **2003**, 2136.
[18] J.-M. Tarascon, M. Armand, *Nature* **2001**, *414*, 359.
[19] P. G. Bruce, B. Scrosati, J.-M. Tarascon, *Angew. Chem.* **2008**, *120*, 2972; *Angew. Chem. Int. Ed.* **2008**, *47*, 2930.
[20] M. Armand, J.-M. Tarascon, *Nature* **2008**, *451*, 652.
[21] D. L. Li, H. S. Zhou, I. Honma, *Nat. Mater.* **2004**, *3*, 65.
[22] K. M. Shaju, P. G. Bruce, *Adv. Mater.* **2006**, *18*, 2330.
[23] F. Jiao, P. G. Bruce, *Adv. Mater.* **2007**, *19*, 657.
[24] K. X. Wang, M. D. Wei, M. A. Morris, H. S. Zhou, J. D. Holmes, *Adv. Mater.* **2007**, *19*, 3016.
[25] P. Poizot, S. Laruelle, S. Grugeon, L. Dupont, J.-M. Tarascon, *Nature* **2000**, *407*, 296.
[26] K. T. Nam, D. W. Kim, P. J. Yoo, C. Y. Chiang, N. Meethong, P. T. Hammond, Y. M. Chiang, A. M. Belcher, *Science* **2006**, *312*, 885.
[27] G. X. Wang, X. P. Shen, J. Horvat, B. Wang, H. Liu, D. Wexler, J. Yao, *J. Phys. Chem. C* **2009**, *113*, 4357.

[28] A. H. Lu, F. Schüth, *Adv. Mater.* **2006**, *18*, 1793.
[29] F. Jiao, A. Harrison, A. H. Hill, P. G. Bruce, *Adv. Mater.* **2007**, *19*, 4063.
[30] K. S. W. Sing, D. H. Everett, R. A. W. Haul, L. Moscou, R. A. Pierotti, J. Rouquerol, T. Siemieniewska, *Pure Appl. Chem.* **1985**, *57*, 603.
[31] W. L. Roth, *J. Phys. Chem. Solids* **1963**, *24*, 1.
[32] E. Salabas, A. Rumplecker, F. Kleitz, F. Radu, F. Schüth, *Nano Lett.* **2006**, *6*, 2977.
[33] S. Takada, M. Fujii, S. Kohiki, T. Babasaki, H. Deguchi, M. Mitome, M. Oku, *Nano Lett.* **2001**, *1*, 379.
[34] C. D. Spencer, D. Schroeer, *Phys. Rev. B* **1974**, *9*, 3658.
[35] T. Ambrose, C. L. Chien, *Phys. Rev. Lett.* **1996**, *76*, 1743.
[36] L. He, C. Chen, N. Wang, W. Zhou, L. Guo, *J. Appl. Phys.* **2007**, *102*, 103911.
[37] W. H. Meiklejohn, C. P. Bean, *Phys. Rev.* **1956**, *102*, 1413.
[38] N. Du, H. Zhang, B. D. Chen, J. B. Wu, X. Y. Ma, Z. H. Liu, Y. Q. Zhang, D. Yang, X. H. Huang, J. P. Tu, *Adv. Mater.* **2007**, *19*, 4505.
[39] X. W. Lou, D. Deng, J. Y. Lee, J. Feng, L. A. Archer, *Adv. Mater.* **2008**, *20*, 258.
[40] X. W. Lou, D. Deng, J. Y. Lee, L. A. Archer, *J. Mater. Chem.* **2008**, *18*, 4397.
[41] L. Tian, H. L. Zou, J. X. Fu, X. F. Yang, Y. Wang, H. L. Guo, X. H. Fu, C. L. Liang, M. M. Wu, P. K. Shen, M. Q. Gao, *Adv. Func. Mater.* **2010**, *20*, 617.

Received: March 4, 2010
Published online: August 5, 2010

